AIAA JOURNAL
Vol. 38, No. 3, March 2000

Mixing of a Sonic Transverse Jet Injected into a Supersonic Flow

Wayne M. VanLerberghe*
The Aerospace Corporation, El Segundo, California 90245
Juan G. Santiago†
Stanford University, Stanford, California 94305
J. Craig Dutton‡
University of Illinois at Urbana–Champaign, Urbana, Illinois 61801
and
Robert P. Lucht§
Texas A&M University, College Station, Texas 77843

The mixing characteristics of an underexpanded sonic jet injected into a Mach 1.6 crossflow are studied experimentally. Shadowgraph photography and planar laser-induced fluorescence from acetone are used to obtain temporally resolved flowfield visualizations of a side view of the barrel shock region, a side view of the downstream plume, and an end view cross section of the plume. Instantaneous images, mean and standard deviation images, and image-intensity probability density functions (PDFs) are used to study the mixing produced by large-scale turbulent structures. PDFs show that time-averaged mixture fraction measurements greatly overestimate the actual level of instantaneous mixing in the flowfield. Comparisons of the instantaneous images and PDFs show the role of large-scale rolling structures and jetlike plumes in transporting coherent packets of fluid across the three-dimensional shear layer formed between the jet and crossflow. Significant instantaneous mixing in this flowfield occurs in the wake region downstream of the barrel shock region and below the jet centerline. The counter-rotating streamwise vortex pair in the jet plume plays an important role in the scalar mixing processes because it transports jet fluid down toward the wake and entrains crossflow fluid from below up into the jet.

Introduction

ENSURING rapid mixing of fuel and air in a supersonic combustor has motivated the study of transverse jet injection into a supersonic flow (TJISF). The highly three-dimensional nature of the TJISF flowfield produces complex mixing processes that are not completely understood. To successfully design supersonic combustors that employ transverse jet injection in some form, a clear understanding of the fundamental mechanisms controlling the supersonic mixing phenomena of a single-jet TJISF is necessary.

Figure 1 (from Ref. 1) shows the flowfield of a typical underexpanded TJISF. As shown, the jet is injected through the bottom wall perpendicular to a supersonic crossflow. The jet obstructs the freestream and induces a bow shock in the flowfield before turning downstream. A horseshoe vortex wraps around the windward side of the jet near the wall and trails downstream of the jet. The underexpanded jet initially expands through a Prandtl–Meyer fan centered at the jet orifice lip and is then compressed through a barrel shock and a Mach disk. Much of the jet fluid passes through the oblique shocks that define the sides of the barrel shock and forms an annular shear layer between the jet plume and the crossflow. Recirculation regions are located just upstream and downstream of the jet orifice near the wall. The velocity field within the jet plume downstream of the barrel shock is dominated by two streamwise-oriented, counter-rotating vortices.

There have been numerous investigations of the flowfields of low-speed and high-speed jets in crossflow,[2] as well as fundamental studies of turbulent mixing phenomena.[3,4] Large-scale coherent structures in turbulent shear layers have been found to have a dramatic influence on mixing and are important in controlling mass, momentum, and heat transport in both high- and low-speed flows.[5] However, compressibility effects can dramatically reduce the growth rate of a shear layer and can affect the characteristics of the large-scale structures within it. These high-speed effects, together with the complexity of the TJISF flowfield, make experimental studies of the mixing phenomena of TJISFs essential.

Early investigations of TJISFs have provided qualitative descriptions of the flowfield structure.[6,7] In addition, several studies have performed parametric investigations of the variables that influence jet penetration and have provided empirically derived relations for penetration.[8,9] Recent studies have also yielded either quantitative or semiquantitative descriptions of the TJISF velocity field.[10–15]

Several investigations have visualized turbulent structures in a transverse jet using either planar Mie scattering or planar laser-induced fluorescence (PLIF).[16–19] Lee et al.[16] studied nonreacting and reacting transverse jets using NO PLIF and OH PLIF, respectively. Hermanson and Winter[17] reported that structures develop at the jet/freestream interface in a periodic manner and persist far downstream of the orifice. Gruber et al.[18] and VanLerberghe[19] found similar large-scale structures. All of these studies produced instantaneous images that showed large-scale turbulent structures that are not apparent in time-averaged images and, therefore, demonstrated the importance of understanding the instantaneous mixing processes.

Several recent investigations have attempted to numerically simulate TJISF by solving the steady, three-dimensional, viscous, compressible, Reynolds averaged Navier–Stokes equations using the Baldwin–Lomax turbulence model.[12,20] Numerical results generally showed good agreement with experimental wall pressure and jet penetration data, but they were usually inadequate for other aspects of the flow, including mixing, details of the velocity field, and jet spreading. These and other studies of TJISF that rely on time-averaged computational or measurement techniques do not provide an accurate description of the instantaneous local mixing states that control reaction rates. The present research program addresses these issues by investigating the instantaneous mixing characteristics of a single transverse air jet injected into a supersonic air crossflow using PLIF from acetone molecules seeded into the jet.

Received 11 December 1997; revision received 20 July 1999; accepted for publication 7 August 1999.

*Senior Member of the Technical Staff. Member AIAA.
†Assistant Professor, Department of Mechanical Engineering. Member AIAA.
‡W. Grafton and Lillian B. Wilkins Professor, Department of Mechanical Engineering. Associate Fellow AIAA.
§Paul Pepper Endowed Professor, Department of Mechanical Engineering. Senior Member AIAA.

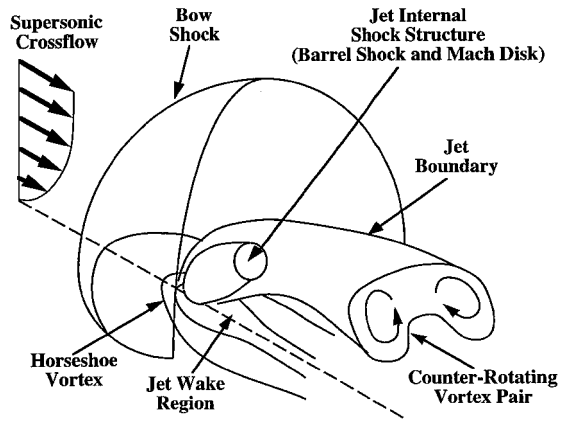

Fig. 1 Perspective view of the three-dimensional flowfield surrounding the transverse injection of an underexpanded jet into a supersonic crossflow (from Gruber[1]).

Experimental Transverse Jet Facility

The experiments presented here were conducted in the Gas Dynamics/Laser Diagnostics Laboratory at the University of Illinois at Urbana–Champaign. The wind tunnel used was designed and built by Carroll[21] and modified for the current effort. The test section is 76 mm wide by 33 mm high. Optical access to the test section is provided by glass windows on the side walls and fused silica windows in the top and bottom walls. The transverse jet nozzle has a 3:5 (minor axis-to-major axis) elliptical contour, is located 211 mm downstream of the $M = 1.6$ nozzle throat, and has an exit diameter of 4 mm. The nozzle was mounted in a countersunk hole in the bottom window to maximize optical access.

The jet-to-crossflow momentum flux ratio J for the results presented here was equal to 1.7. The freestream crossflow air had a Mach number of 1.6, a stagnation pressure of 241 kPa, and a stagnation temperature of 295 K (resulting in a unit Reynolds number of 58.8×10^6 m^{-1}). The air jet stagnation pressure, stagnation temperature, and Reynolds number based on jet diameter for the current measurements were $P_{0j} = 476$ kPa, $T_{0j} = 300$ K, and $Re_d = 1.1 \times 10^5$.

The acetone for PLIF was injected only into the transverse jet flow using atomization nozzles placed far upstream of the test section. The flowrate of acetone was controlled using Aalborg flowmeters. The acetone vapor saturation levels for the jet cases investigated here can be calculated by a fit of the Antoine equation suggested by Lozano et al.[22] For the present $J = 1.7$ flow conditions, the jet is predicted to become saturated at an acetone seeding level of approximately 6600 ppm. The actual acetone seeding level used was approximately 9400 ppm to increase the relatively low PLIF signal levels. Despite this supersaturated state, minimal acetone condensation was observed in the flowfield.

PLIF Imaging

Acetone PLIF has been applied successfully in various flow studies, including transverse jets injected into a subsonic crossflow.[22–24] A short description of acetone PLIF will be given here, whereas a detailed description, including a discussion of the photophysics of acetone, can be found in Refs. 22 and 23.

The absorption spectrum of acetone molecules (CH_3–CO–CH_3) is broadband, ranging from 225 to 320 nm, and peaks at 270–280 nm. In our acetone PLIF studies, we used the fourth harmonic radiation from a Q-switched Nd:YAG laser at 266 nm for which the acetone absorption cross section is 4.4×10^{-20} cm^2 (approximately 7% below the maximum value). The acetone laser-induced fluorescence spectrum, that is, the desired signal, is also broadband, ranging from 350 to 650 nm, with peaks at 445 and 480 nm. Breuer and Lee[25] measured an acetone fluorescence lifetime of 1.7 ± 0.3 ns with 280-nm excitation. Consequently, the temporal resolution of the current experiments is limited only by the 6–8 ns Nd:YAG laser pulse.

Laser illumination was provided by a Continuum Model NY81C-10, pulsed Nd:Yag laser with a maximum repetition rate of 10 Hz. A fourth harmonic crystal was used to provide output beams at 266 nm with a maximum pulse energy of 100 mJ. The laser beam was focused into a sheet about 50 mm wide and 250 μm thick by a spherical lens ($f = 500$ mm), a negative cylindrical lens ($f = -19$ mm), and a positive cylindrical lens ($f = 150$ mm). Given these laser sheet characteristics, the 100-mJ pulse energy was well below the saturation level of acetone fluorescence.[22] Mirrors were used to orient the sheet in the streamwise vertical (side-view) and spanwise vertical (end-view) planes shown in Fig. 2.

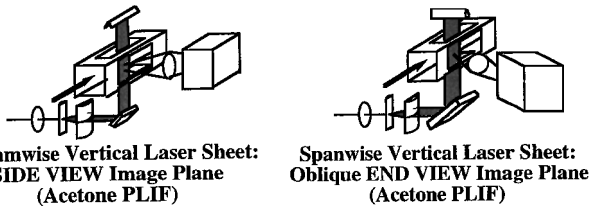

Fig. 2 Schematic of wind-tunnel test section, camera, and laser-sheet orientations showing optical train and imaging views.

The fluorescence images were recorded using a Photometrics, Ltd., digital charge-coupled device (CCD) camera system, a Photometrics AT 200 controller (14-bit A/D), and a thermoelectrically cooled (−40°C) CH250 camera head with a Tektronix TK512CB/AR CCD detector array. The CCD array is a thinned, back-illuminated CCD sensor with a 512×512 array of square pixels, each with an edge dimension of 27 μm. A micro-Nikkor 105-mm, $f/2.8$ Nikon camera lens was used to obtain end-view images, and a Nikkor 50-mm, $f/1.4$ camera lens was used to obtain side-view images. Photometrics PMIS software was used to acquire and process the images; additional image processing was performed using Spyglass Transform software and custom FORTRAN programs.

In the current PLIF experiments, acetone tracer molecules absorb incident photons provided by the laser sheet and are excited to a higher energy level. These excited molecules return to their ground state via radiative processes, such as fluorescence and phosphorescence, and nonradiative decay processes, such as dissociation, collisional quenching, intersystem crossing, and internal conversion. In the present airflow, phosphorescence phenomena are strongly quenched by oxygen and are not expected to interfere with the fluorescence signal. Because collisional quenching is expected to be negligible in this low-pressure airflow, the fluorescence quantum yield is assumed to be relatively independent of molecular collisions. Instead, the acetone fluorescence quantum yield is expected to be dominated by intersystem crossing and, therefore, is proportional to the local acetone molecular number density.

Given the velocity measurements in this flowfield by Santiago and Dutton,[13] the maximum value of the crossflow-to-jet-fluid static temperature ratio (T_c / T_j) throughout the flowfield is expected to be less than 1.4. Because gas density is inversely proportional to temperature, jet fluid partial densities calculated from measured intensity ratios, $I / I_{\max}$, will be lower than the actual values in high-temperature regions. Taking only this temperature effect into account, we estimate that the measured fluorescence signal $I / I_{\max}$ underpredicts the actual value of the jet fluid mixture fraction (by mass) ξ by a maximum absolute error of about 0.084 at $\xi = 0.54$ or a relative error of approximately 15% (Ref. 19).

In addition to the signal dependence on density, the acetone fluorescence quantum efficiency can vary significantly with both temperature and pressure. A measurable dependence of quantum efficiency on temperature has been reported by several authors.[26–30] The static temperature values in the barrel shock region of the TJISF flowfield range from 123 K (immediately preceding the Mach disk) to 281 K (immediately downstream of the Mach disk).[13,15] An extrapolation of the low-temperature data of Bryant et al.[30] suggests a reduction in acetone quantum efficiency (as temperature decreases) of approximately 16% over this temperature range.

The pressure dependence of quantum efficiency has also been investigated[26–31] and is currently a subject of debate. Whereas Ghandhi and Felton,[26] Lee and Santavicca,[28] and Bryant et al.[30] reported no discernible pressure dependence for their experimental conditions, the measurements of Grossmann et al.,[27] Ossler and Alden,[29] and Yuen et al.[31] clearly show that quantum efficiency

increases with increasing pressure. For example, Yuen et al.[31] investigated four different buffer gases and found that, when the buffer gas was air, there was a 30–50% increase in the acetone fluorescence quantum efficiency as pressure was increased from 0.6 to 5 atm. In comparison, the static pressure values in the barrel shock region of the TJISF flowfield range from 0.22 atm (immediately preceding the Mach disk) to 2.5 atm (at the jet exit).[13,15] A simple extrapolation of the data of Yuen et al.[31] yields a quantum efficiency increase of approximately 40% over this pressure range.

The pressure and temperature dependence of the quantum efficiency, together with the effects of mean density on the signal strength, show that the current measurements of local acetone molecular number density are only an approximate measure of the partial density of jet fluid. However, note that the factors affecting signal intensity partially offset each other in some cases. For example, through adiabatic compressions, signal strength decreases with increasing temperature because of the dependence on partial jet density. In contrast, the signal strength in these cases tends to increase as a result of the temperature and pressure dependences of quantum efficiency. Also, the uncertainty in relating local acetone molecular number density to partial density of jet fluid is much less severe in regions where mixing occurs (in the annular shear layer between the jet and crossflow and the jet wake region). Thus, despite these features of the acetone PLIF method, many important observations can be made concerning the mixing processes in this flowfield. In particular, we can use these measurements to study the locations of important mixing regions, make comparisons between time-averaged and instantaneous mixing, investigate the role of large-scale structures in mixing, and approximate the degree of mixing in the shear layers of the flowfield.

The spatial resolution L of the imaging system utilized in these experiments was calculated from the modulation transfer function (MTF) of the system. The spatial resolution is defined by the cutoff spatial frequency at which the MTF falls to 4% of its peak value and specifies the minimum resolvable size, that is, smallest flow scale, that can be distinguished by the imaging system. The MTF for this imaging system is specified by both the CCD array and the collection lens. The spatial resolution for the images presented here are $L = 0.19$ mm for the side view of the barrel shock region, 0.20 mm for the side view of the downstream plume, and 0.47 mm for the end view. Note that these spatial resolution length scales are roughly 500 times larger than the estimated Batchelor scales for this flowfield.[19] Therefore, the mixing processes observed here are at large turbulent scales, that is, stirring, which is the first step in the cascade of turbulent scales that leads to mixing at the molecular level.[32,33]

Camera dark current, background effects due to reflections, and window fluorescence were removed by subtracting a scaled average background image from every raw image. Each image was then normalized by a laser sheet correction image to account for spatial variations in the laser sheet energy and variations in the camera response from pixel to pixel.

Results and Discussion

The following sections present and discuss a shadowgraph flow visualization, representative instantaneous PLIF images, mean and standard deviation PLIF images, and probability density functions (PDFs) based on PLIF image ensembles. The images are presented for the side-view and end-view orientations shown in Fig. 2.

Shadowgraph Flow Visualization

Figure 3 shows a representative shadowgraph image of the TJISF flowfield for the $J = 1.7$ case investigated here. In this image, the crossflow travels from left to right, and the jet is injected through the bottom wall. The bow shock, boundary-layer separation shock, barrel shock, and Mach disk are clearly visible in the image. The jet boundary is less clear, but large-scale turbulent structures are evident, although their characteristics are smeared by the line-of-sight integrating nature of the shadowgraph method. The reflection of the bow shock from the top wall of the test section is also visible. Superimposed shadowgraph images taken at random times suggest that there is little or no bow shock movement even in the area near the top wall where the bow shock is reflected.

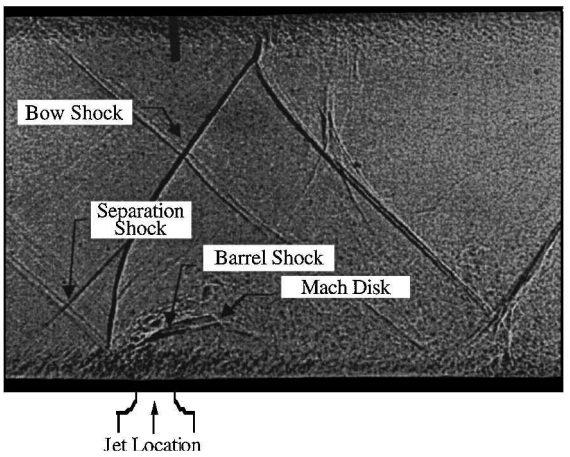

Fig. 3 Shadowgraph image of the TJISF flowfield.

Instantaneous PLIF Images

At least 180 acetone PLIF images were obtained for each of the flowfield views presented. Although imaging was also performed at $J = 1.2$ and 2.2 (Ref. 19), because of space limitations, only the $J = 1.7$ results are presented here as a representative, nominal case. All images use a linear gray scale in which white corresponds to the highest signal level. The gray-scale range was selected separately for each set of images to maximize contrast. Also, the images were acquired at random times so that there is no time correlation between them.

Figures 4a, 4b, and 5 each show three representative instantaneous images of the TJISF flowfield for a side view of the region near the barrel shock, a side view of the plume downstream of the barrel shock, and an end view, respectively. These views extend throughout the following domains, where x, y, and z are in the streamwise, transverse, and spanwise directions and the origin is at the center of the jet exit: $z/d = 0$ side view (near barrel shock region), $x/d = -1$–4.2 and $y/d = 0$–4; $z/d = 0$ side view (downstream of barrel shock), $x/d = 2$–7 and $y/d = 0$–4.1; and $x/d = 2$ end view, $y/d = 0$–3.5 and $z/d = -2.2$–2.2.

Instantaneous Side View of Barrel Shock Region

As in all of the images of the inner jet region obtained in this study, Fig. 4a clearly shows the outline of the barrel shock and Mach disk. The shape and position of the downstream edge of the barrel shock are consistent from image to image. However, the shape of the upstream edge of the barrel shock shows a degree of unsteadiness, occasionally fluctuating from image to image. This edge usually takes the form of a smooth convex curve but, less frequently, looks rather distorted. For example, at times the upstream edge is flattened into two or more approximately straight segments that join at sharp corners (see the middle image in Fig. 4a). At other times, a portion of the upstream edge displays an indented or rippled nature.

A notable similarity in all of the images of the barrel shock region is the parabolically shaped high-intensity region in the jet immediately outside the injector. Because there is no mixing inside the barrel shock region, the acetone signal intensity is roughly directly proportional to the fluid density of the jet injectant (assuming no pressure effect on quantum efficiency). The parabolic density distribution results as the exiting high-pressure jet fluid is rapidly expanded by a series of expansion waves centered at the orifice lip. The fluid density (and the corresponding signal intensity) in the barrel shock region decreases further in the streamwise direction along the jet centerline and is lowest immediately upstream of the Mach disk. Also, the signal intensity immediately outside the barrel shock is much higher than that from the adjacent region inside, due to the significant increase in density as the fluid passes through the barrel shock. Mixing occurs only in the shear layer outside the barrel shock.

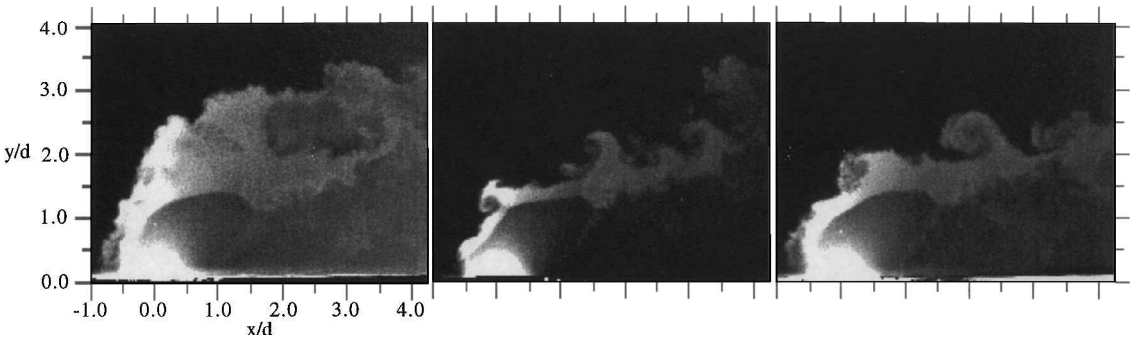

Fig. 4a Representative instantaneous images of the side-view barrel shock region.

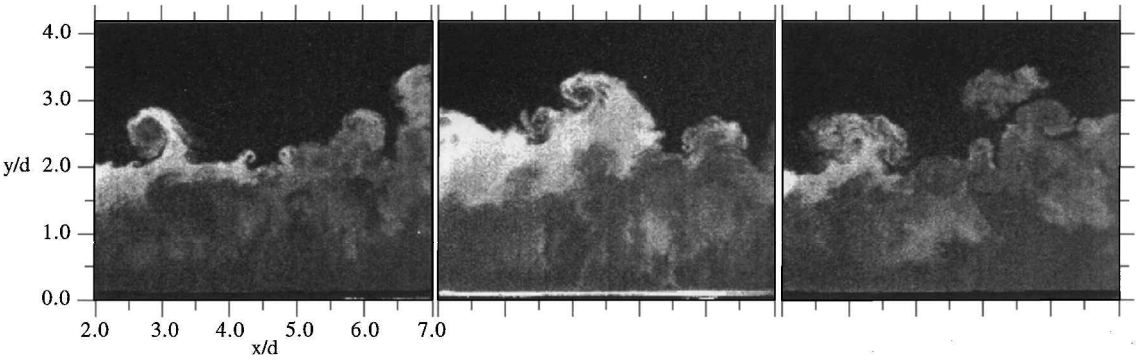

Fig. 4b Representative instantaneous images of the side-view downstream region ($x/d = 0.0$ is the center of the jet).

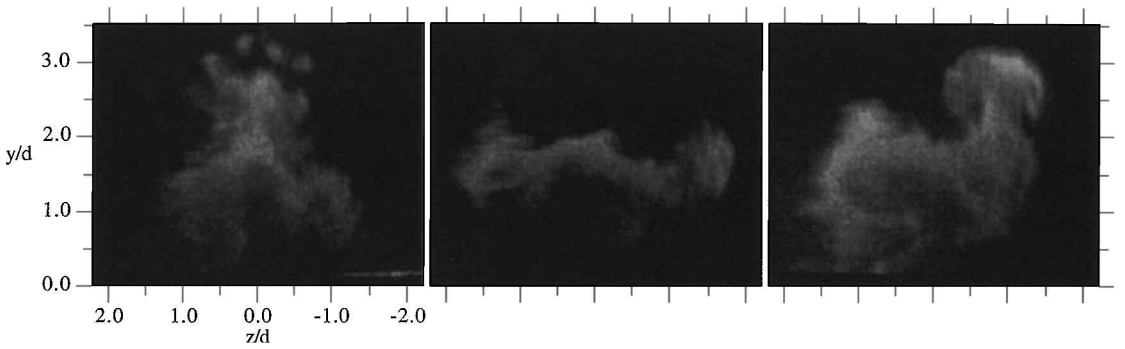

Fig. 5 Representative instantaneous images from the end view of the jet plume at $x/d = 2$.

In most cases, a considerable amount of jet fluid bypasses the Mach disk through the upstream edge of the barrel shock, for example, the left-hand image in Fig. 4a. Because this fluid retains much of its momentum, it can continue to penetrate far into the crossflow. Some instantaneous jet structures were observed to achieve a maximum penetration height two to three times the height to the center of the Mach disk. The largest vortices usually appeared to be formed by jet fluid that bypassed the Mach disk and mixed with the crossflow at high velocities. In most cases, the structures at the upper shear layer edge appear to roll up counterclockwise into the crossflow, which indicates that the jet fluid has the higher velocity at this interface.

The structures along the lower edge of the jet appear to be less organized and extend periodically far down toward the wall in the wake region immediately below and downstream of the barrel shock region. Generally, these structures are much less distinct than the structures along the upper edge of the jet. The intermediate signal levels in the wake region indicate that considerable mixing between the jet and crossflow fluid may occur there. This subject will be discussed later in relation to the PDFs.

One of the most striking characteristics among the instantaneous images presented is the dramatic variation they exhibit with respect to each other. Variations in the size, shape, and periodicity of the dominant large-scale turbulent structures on the upper jet edge are readily apparent. These structures often penetrate far into the crossflow and engulf large amounts of crossflow fluid. The location of the jet boundary and the extent of jet penetration also differ substantially between images for the same jet case.

Instantaneous Side View of Downstream Plume

Figure 4b shows three representative side views of the plume just downstream of the barrel shock region. Again, the images provide excellent, qualitative visualizations of the variation in turbulent structures in the plume. Much of the jet boundary is nearly horizontal, that is, parallel to the crossflow, in many of the images, although the boundary is at different heights at different instants, and large-scale structures extend up out of the main jet boundary on a regular basis. In many ways the flowfield in this region is similar to that of a planar mixing layer.

As in the case of the side view of the barrel shock region, most of the upper edge structures seem to be rolling up counterclockwise into the crossflow, which again suggests that the jet fluid at this boundary is moving faster than the crossflow fluid at that location. However, a few structures, for example, at $x/d = 4$ in the left-hand image of Fig. 4b, seem to be rolling up in the opposite direction (clockwise), indicative of crossflow fluid that is locally faster than

the jet fluid. Such trends concerning rotation direction have also been observed by Gruber et al.[18] in the TJISF flowfield and by investigators of planar shear layers.[3,34] In some cases, mushroom-shaped structures protrude upward out of the jet and into the crossflow (see the right-hand image of Fig. 4b). These mushroom-shaped structures probably consist of a vortex ring and represent jetlike plumes ejecting jet fluid across the mixing layer.

The wake region near the wall is visualized much more clearly in these images than in those from the barrel shock region. Again, the intermediate signal levels in the lower portion of this region indicate that good mixing has probably occurred in the wake. The wake structure lacks any dominant large-scale organization, but vertically oriented fingerlike structures of jet fluid can be seen to reach down toward the wall. These fingerlike wake structures are most prevalent after the jet has completed most of its turning and are absent nearer the injector where the jet is turning considerably. In contrast to our observations for a compressible jet in crossflow with $J = 1.7$, Smith and Mungal[24] observed jet fluid in the wake only for subsonic, incompressible jets in crossflow with values of J above 100.

Instantaneous End View

Because optical access for the end views was available only through the side windows, the camera was placed at an oblique angle to acquire the spanwise vertical image plane (see Fig. 2). This configuration resulted in lower spatial resolution than for the side views because the aperture setting required to maximize the PLIF signal reduced the focal depth of the imaging system. Consequently, regions far from the center of the image are slightly out of focus. In addition, this imaging configuration resulted in a geometrical distortion of the end view of the plume. This distortion is similar to trapezoidal distortion and occurs because regions closest to the imaging lens are magnified more than regions farther away. The geometrical distortion in the images for each end-view ensemble was removed using a postprocessing image correction technique.[19]

Figure 5 shows three typical instantaneous images of the end view of the plume at $x/d = 2$. The jet boundary and large-scale structures of the end-view images are less clearly defined than those in the side views for the reasons just stated, which results in a lower signal-to-noise ratio for these images. Note that there is a region of zero intensity along the lower edge of the images that extends across their entire spanwise extent (most noticeable in the rightmost image) because one of the wind-tunnel walls partially blocked the camera's view of the illuminated flowfield region.

A common feature of the end-view images is the crescentlike shape of the plume cross section. This shape is indicative of a counter-rotating streamwise vortex pair of the plume and is comparable to the jet cross sections observed in other studies of compressible transverse jets.[6,17,18] This vortex pair advects unmixed crossflow fluid up into the bottom of the plume.

As in the other views, the instantaneous end-view images in Fig. 5 display considerable variation from image to image. Large-scale structures vary in size and location along the jet boundary but usually contain a considerable amount of jet fluid, that is, high signal intensity. At this $x/d = 2$ location, the plume cross section is usually asymmetric and skewed toward the upper right at a small angle with respect to the bottom wall (see following discussion of the mean image). In addition, the left vortex generally appears larger than the right vortex. Smith and Mungal[24] and Santiago and Dutton[13] observed similar asymmetric behavior of the vortex pair in jets in crossflow.

End-view images at $x/d = 1$ (not presented here) show that much of the jet fluid passes through the sides of the barrel shock and bypasses the Mach disk. This is an important observation because jet fluid that passes through the Mach disk loses most of its momentum. Several of the large-scale mushroom-shaped structures that are captured in the end views penetrate as far as one jet diameter away from the jet cross section. (See the right-hand image of Fig. 5 for a realization of a very large mushroom structure.) This deep penetration is not surprising because these structures likely contain high-momentum jet fluid that has accelerated strongly through the jet core and has been only weakly decelerated as it passed through the barrel shock at an oblique angle. Similar observations were made in the side-view images.

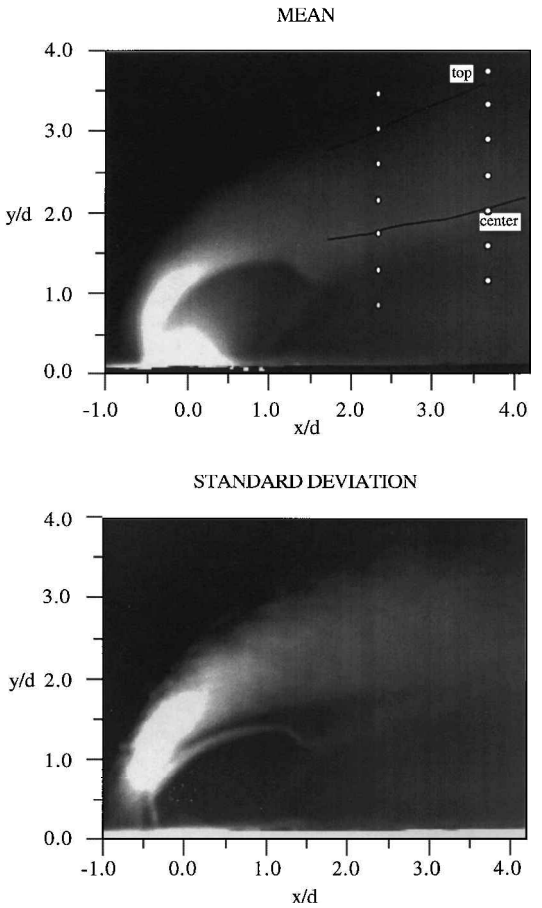

Fig. 6 Mean and standard deviation images for the side-view barrel shock region ensemble: circles overlaid on the mean image mark the locations at which PDFs were calculated; $x/d = 0.0$ is the center of the jet.

Mean and Standard Deviation PLIF Images

Figures 6–8 show the mean and standard deviation images for the side view of the region near the barrel shock, the side view of the downstream plume, and the end view of the plume, respectively. The statistics for each case are based on at least 180 instantaneous images, although 270 images were used in the case of the side view of the barrel shock region. The circles overlaid on each mean image mark the approximate locations at which PDFs were calculated for each image ensemble (to be presented and discussed later).

Mean and Standard Deviation Images of Side View of Barrel Shock Region

Figure 6 shows the mean and standard deviation images for the side view of the region near the barrel shock. The overlaid line labeled center corresponds to the mean trajectory of the jet centerline downstream of the Mach disk, defined by the location of the maximum intensity level at each streamwise position. The line labeled top on each image corresponds to the upper boundary of the jet, defined as the locations at which the intensity has decreased to 30% of the maximum at each streamwise position.

Many of the trends observed in the instantaneous images are confirmed by the mean and standard deviation images. The shape of the barrel shock and the height of the Mach disk are readily apparent in the mean image. A high-intensity region in the standard deviation image outlines the windward side of the barrel shock and the Mach disk. The much lower intensity outline on the leeward edge of the barrel shock in the standard deviation image indicates that it probably fluctuates to a much smaller degree than either the upstream edge or the Mach disk. However, the low absolute signal levels in the regions on both sides of the downstream edge (apparent from the mean images) are at least partially responsible for the low value of standard deviation there.

In the mean image of Fig. 6, the parabolic density profile of the jet fluid immediately outside the jet exit is again apparent. As

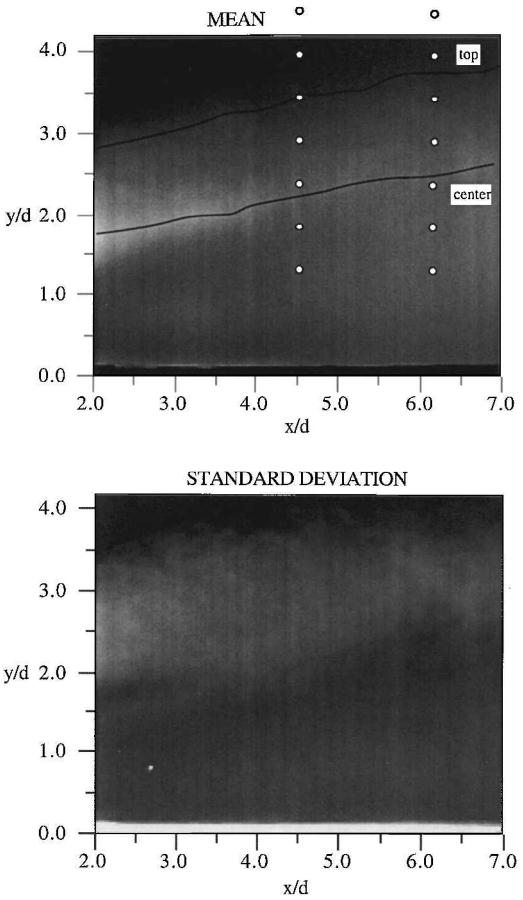

Fig. 7 Mean and standard deviation images for the side-view downstream region ensemble: circles overlaid on the mean image mark the locations at which PDFs were calculated.

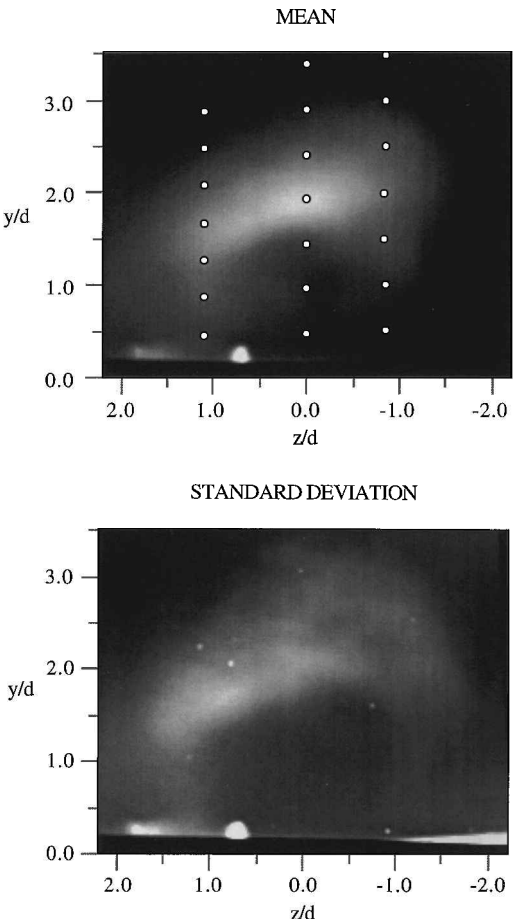

Fig. 8 Mean and standard deviation images for the end-view ensemble: circles overlaid on the mean image mark the locations at which PDFs were calculated; $x/d = 0.0$ is the center of the jet.

mentioned earlier, this parabolic density distribution in the jet core results from of a series of expansion waves propagating from the edges of the jet orifice; that the standard deviation in this region is very small (almost completely black in the standard deviation image) indicates that the expansion processes within the jet core are quite steady. This is not surprising because the fluid dynamic processes affecting the supersonic jet fluid within the region bounded by the barrel shock should not be influenced by small disturbances outside the barrel shock.

The region just upstream of the windward side of the barrel shock and roughly 1–2 jet diameters from the wall shows a high intensity in both the mean and standard deviations images. In the mean image, this is indicative of the very high-density jet fluid that did not expand significantly before traversing the barrel shock. In the standard deviation image, this high intensity indicates the highly intermittent nature of the large turbulent structures that occur in this region. Likewise, the relatively high standard deviation level throughout the mixing region at the top of the jet plume shows the intermittent nature of the structures along the entire jet–crossflow shear layer.

Mean and Standard Deviation Images of Side View of Downstream Plume

Figure 7 shows the mean and standard deviation images of the region downstream of the barrel shock. The mean image shows that, downstream of the Mach disk, the mean jet centerline and top boundary of the jet continue to rise at approximately the same rate for as far as seven jet diameters downstream of the jet exit. This is despite the upper edge of the jet appearing to be fairly horizontal in many of the instantaneous images (recall Fig. 4b). Apparently, there is also significant mixing in the wake region below the main jet plume. The mean signal level in this region near the wall approaches the level at the centerline toward the right edge of the image. Again, the high standard deviation levels above the jet centerline indicate considerable intermittency in the large-scale structures along the upper jet boundary.

Mean and Standard Deviation Images of End View

Figure 8 presents the mean and standard deviation results for the $x/d = 2$ end-view image ensemble. Figure 8 shows that the mean jet cross section is generally fuller than was indicated by the corresponding instantaneous jet cross sections but that it is still crescent shaped to some degree. The mean jet cross section is much more similar to the classical kidney-shaped transverse jet cross sections observed in other studies[6,14,17,18] than were the corresponding instantaneous cross sections shown in the preceding section. In the present study, the mean jet cross sections clearly show round nodes on both sides of the jet centerline that indicate the presence of the streamwise vortex pair. On the basis of the mean image, it is difficult to conclude definitely that one vortex is larger than the other.

The mean jet cross section does show significant asymmetry, about the $z = 0$ plane. Although not presented in this paper, images obtained at $x/d = 1$ and 3, as well as the present $x/d = 2$ images, show that the jet plume cross section is roughly symmetric in the barrel shock region, becomes skewed and asymmetric at $x/d = 2$, and then returns to a more symmetric nature at $x/d = 3$. This asymmetry just downstream of the barrel shock region and the trend toward a symmetric cross section farther downstream was also observed in the velocity measurements of Santiago and Dutton[13,14] that were performed in the same facility and at the same conditions as the present study. The cause for this asymmetry immediately downstream of the Mach disk is unclear. Possibly, the transverse jet is most susceptible to asymmetric flow disturbances in the highly complex, three-dimensional region just downstream of the barrel shock. Smith and Mungal[24] also observed asymmetric jet cross sections in both the instantaneous and mean cross sections of incompressible transverse jets.

In the standard deviation image of the plume cross section, high standard deviation levels occur in a large region near the top and sides of the plume cross section. Again, this confirms the fluctuating

nature of the turbulent structures of the annular shear layer between the jet and the crossflow. Note that these high standard deviation levels are probably due to the intermittent expulsion of jet fluid into the crossflow by large-scale structures, and therefore, the mean image overestimates the level of mixing in these regions.

There are low standard deviation levels in the region below the center of the jet, even though instantaneous signal intensities in this region are sometimes relatively high (see Fig. 5). This low standard deviation indicates that the instantaneous jet fluid density, that is, signal level, is constant over time in this region. Finally, note that the spots of high standard deviation near the lower wall are merely indications of high levels of background noise in this region.

PDF Procedure

Comparisons of instantaneous images with mean images show the dramatic difference between the instantaneous and time-averaged levels of mixing throughout the TJISF flowfield. Large packets of mostly unmixed fluid are often transported across the mixing layer in an intermittent manner by large-scale structures, and time-averaged results alone are, therefore, not sufficient to describe mixing in this flowfield. For this reason, PDFs of the signal intensities were calculated at various locations in the flowfield. These PDFs show the probabilities of specific instantaneous intensity levels occurring at these locations. Because the signal intensity is directly proportional to the number density of acetone molecules in the jet fluid, the PDFs provide an indication of the instantaneous mixture composition within various regions of the flowfield, although on a pixel-sized stirring basis.

PDFs were calculated at several specific locations for each of the side- and end-view image ensembles, as shown in Figs. 6–8. These locations were selected to provide a good representation of the instantaneous mixing characteristics across the major mixing regions of the annular shear layer between the jet and crossflow. For the side views, individual PDFs were calculated at each of seven transverse locations that were evenly distributed along four vertical lines that spanned the entire extent of the mixing layer (or jet plume) to be examined. For the end view, the PDF locations were evenly distributed along three vertical lines that spanned the entire extent of the plume cross section; seven transverse locations were again used in this case. The center PDF (in the transverse direction) was calculated where the maximum mean intensity occurred (usually the center of the jet), and the outermost PDFs were calculated where the mean intensity profile became relatively constant (well outside the jet boundary).

The individual PDFs were constructed from discrete intensity histograms at each location, and each histogram was composed of equally sized bins. The final ensemble histogram at each flowfield location was generated from an 11×11 pixel region surrounding that location to obtain a statistically sufficient number of samples. Thus, the histograms for the ensembles with 180 images were based on 21,780 individual intensity samples. The 270 image ensembles likewise had 32,670 samples. For clarity, the intensity values, I/I_{max}, are normalized by the highest signal level in the entire vertical traverse.

By definition, the probability values are normalized such that the integrated area beneath each PDF equals unity. These probabilities are plotted as a function of the normalized intensity I/I_{max}. All probability values greater than four (which occur only at the edges of the profiles) have been clipped for the purpose of clarity. The PDFs for each vertical traverse are grouped in columns, and the location of maximum intensity in the mean image, that is, the jet center, is noted for each traverse.

PDF Results

Figures 9–11 present the computed PDFs for the side view of the region near the barrel shock, the side view of the plume downstream

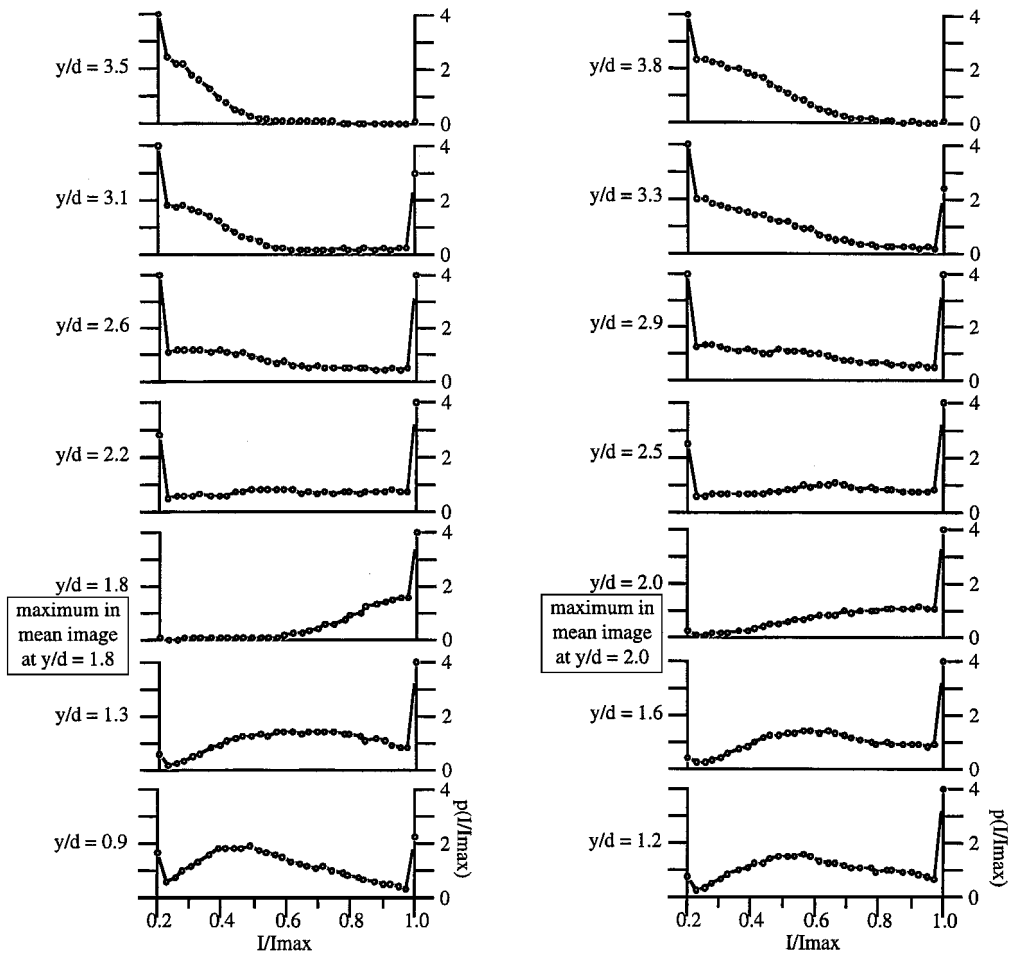

Fig. 9 PDFs from the side-view barrel shock region image ensemble.

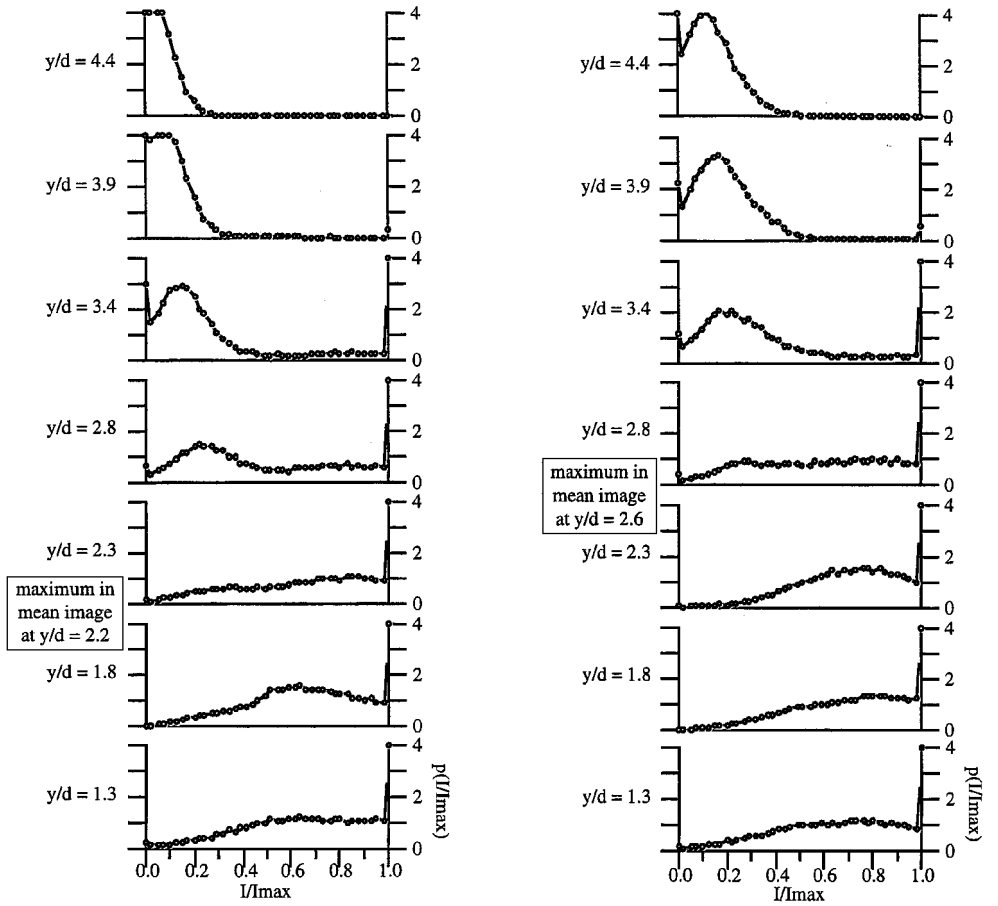

x/d = 4.5 *x/d* = 6.1

Fig. 10 PDFs from the side-view downstream region image ensemble.

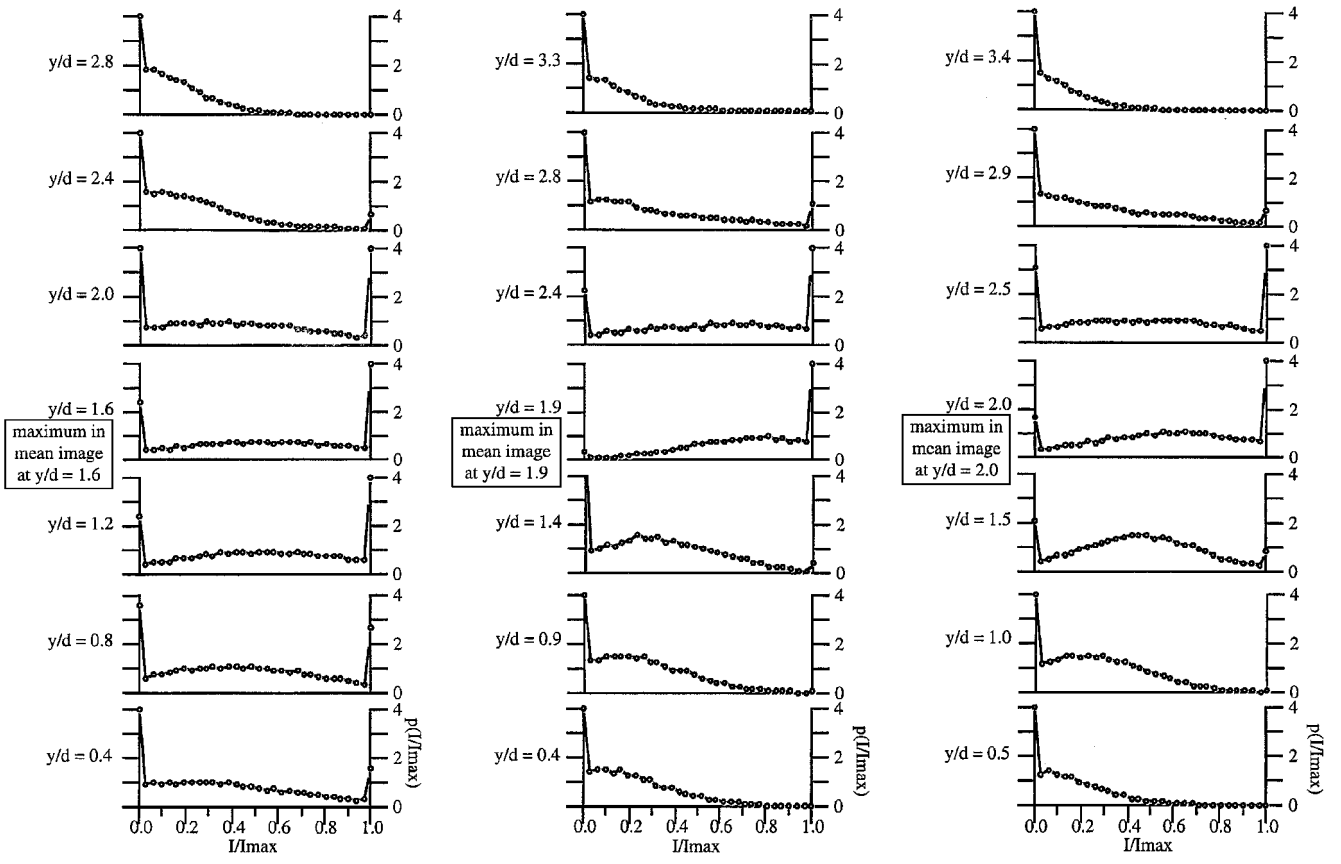

z/d = 1.1 *z/d* = 0.0 *z/d* = − 0.8

Fig. 11 PDFs from the *x/d* = 2 end-view image ensemble.

of the barrel shock, and the end view, respectively. It is useful to refer back to Figs. 6–8 (mean images) to determine the locations of the PDFs with respect to the mean flowfield structure and mixing layers. In these PDF plots, high-probability values at intensity ratios of approximately zero indicate nearly unmixed crossflow fluid. Conversely, high-probability values at intensity ratios near unity indicate nearly unmixed jet fluid. As mentioned earlier, the intensity ratios (measurements of local acetone molecular number density) are an approximate measure of the partial density of jet fluid.

PDFs in Barrel Shock Region

Figure 9 presents PDFs for two streamwise locations ($x/d = 2.3$ and 3.7) in the barrel shock region that span the jet cross section from the freestream above the jet centerline to the wake region below. First, note the trends in the PDFs at $x/d = 2.3$ as the jet is traversed from high to low y/d values. The results from $y/d = 3.5$ to 1.8 represent a traverse of the top half of the jet and include the top portion of the annular shear layer between the jet and the crossflow. At large values of y/d, the PDF peak at small values of I/I_{max} indicates mostly unmixed crossflow fluid. As y/d decreases, the probability of unmixed crossflow fluid (near zero I/I_{max}) decreases and the probability of intermediate I/I_{max} ratios (mixed fluid) increases. At the same time, the appearance of a sharp peak near $I/I_{max} = 1.0$ signals the intermittent presence of unmixed jet fluid. Throughout the shear layer region above the jet centerline, the probability of intensity ratios near 0.5 remains relatively low. This trend shows the relatively low probability of well-mixed fluid occurring in the top portion of the shear layer between the jet and crossflow. Next, note the shape of the PDF curves for y/d values below the jet centerline. As y/d is decreased to 1.3 and 0.9, the PDF measurements show a region of good mixing with relatively high probabilities in the intermediate intensity ratio range of $I/I_{max} = 0.4$–0.7.

The PDF curves at $x/d = 3.7$ show a similar trend. In the shear layer above the jet, the curves are predominantly bimodal with two peaks at the intensity ratio extremes and relatively low values in the intermediate range of 0.3–0.7. In the shear layer below the jet, however, a distinct local maximum of probability values at intermediate intensity ratios is seen to traverse slowly from right to left (high to low intensity, indicating decreasing jet fluid concentration) as y/d decreases.

The PDFs in the barrel shock region, therefore, show that mixing between the jet and the crossflow occurs mainly in the region below the jet. The significant difference between the rate of mixing at the top and the bottom of the jet can be attributed to the three-dimensional structure of the transverse jet flowfield. For example, the velocity differences and convective Mach numbers associated with the top of the annular shear between the jet and crossflow are much larger than those below. Also, as shown by the velocity measurements of Santiago and Dutton,[13,14] the vertical motion associated with the streamwise, counter-rotating vortices is much more vigorous near the bottom half of the jet than the top.

PDFs in Downstream Plume

Figure 10 presents PDFs that span the jet cross section at two streamwise locations ($x/d = 4.5$ and 6.1). At these downstream locations, the maximum mean image intensity, that is, the jet centerline, has moved up to about $y/d = 2.2$ and 2.6, respectively. The trends shown by the PDFs at these locations are similar to those closer to the jet exit. At the top edge of the plume, the PDFs again show a peak near $I/I_{max} = 0.0$ (unmixed crossflow fluid), as expected. At both streamwise locations, the probability peaks at low-intensity values are now slightly wider. This widening is indicative of the mixing caused by turbulent diffusion as the jet develops; the fluid at these locations is usually unmixed crossflow but has some jet fluid periodically entrained. Near the jet centerline, a range of nearly constant and relatively low probability is seen from $I/I_{max} = 0.2$–0.9 with a peak near $I/I_{max} = 1.0$, which shows high probability of unmixed jet fluid. In the lower region of the shear layer (at y/d values below that of the maximum mean image intensity), the PDFs again show relatively high probabilities at intermediate, that is, well-mixed, intensity ratios.

An important difference between the PDFs shown in Fig. 10 and those of Fig. 9 is the lack of high probabilities of unmixed crossflow fluid, that is, at very low I/I_{max} values, in the region below the jet. This indicates that relatively small amounts of unmixed crossflow fluid persist between the jet centerline and the lower wall as the jet develops.

Qualitatively, the PDFs in the downstream plume of our compressible jet in crossflow are somewhat different from those reported by Smith and Mungal[24] for the incompressible case. For example, although the PDFs of the latter authors also show a distinctive unmixed jet peak near $I/I_{max} = 0.0$ that disappears as the jet centerline is approached, their incompressible flowfield measurements show a distinct maximum in I/I_{max} at the centerline. This is in contrast to our relatively constant value of I/I_{max} near the jet centerline.

PDFs in End View

PDFs for the end-view cross section of the jet at $x/d = 2$ are shown in Fig. 11. This cross section cuts through the jet just downstream of the Mach disk (see Figs. 4a and 6). PDFs are presented for seven transverse locations at each of the three spanwise positions, $z/d = 1.1$, 0.0, and -0.8, that span the jet cross section. For these three spanwise locations, the maximum mean intensities occur at $y/d = 1.6$, 1.9, and 2.0, respectively. The center column of PDFs (labeled $z/d = 0.0$) can be compared to the $x/d = 2.3$ PDFs of Fig. 9. The $z/d = 0.0$ PDFs in Fig. 11 lie a distance of just 0.3 jet diameters upstream of the $x/d = 2.3$ PDFs of Fig. 9. The present $z/d = 0.0$ curves show trends very similar to the first column of Fig. 9; the reader is referred to the earlier discussion of Fig. 9.

Figure 11 confirms many of the trends already observed in the side-view PDFs. Poor mixing persists in the region above the center of the jet, as shown by low probabilities of well-mixed fluid at intermediate intensity ratios. Also, high peaks on both wings of most of the PDFs show high probabilities of both unmixed jet fluid and unmixed crossflow fluid at the same location simultaneously. The greatest level of mixing generally occurs below the jet center. Furthermore, the mixing in the region between the streamwise vortices, $z/d = 0.0$, is just slightly better than the mixing below the center of the vortices, on either side. However, high probabilities of unmixed crossflow fluid are indicated at every location below the jet. This supports the expectation that the streamwise vortex pair acts to draw crossflow fluid up into the center of the jet.

High probabilities of unmixed jet fluid are also shown below the jet but only at certain locations. This suggests the presence of large-scale structures that extend out from the jet boundary at these locations, that is, the left vortex in this case. The asymmetry of the jet cross section that was apparent earlier in the instantaneous and mean end-view images at this location is verified by the end-view PDFs in this manner. Note the differences between the PDFs in the left and right columns of Fig. 11 below the location of the mean intensity maximum.

Conclusions

The PDFs presented show that time-averaged mixture fraction measurements greatly overestimate the actual level of instantaneous mixing in the TJISF flowfield. The present measurements clearly show that there are regions in the flowfield where the probability of well-mixed fluid is very low on an instantaneous basis, yet the corresponding location in the mean image shows an intermediate gray-scale level that wrongly suggests a higher level of mixing. Furthermore, these PDFs corroborate the information gained from the instantaneous images. The large-scale rolling structures that were observed to periodically pass through the mixing layer are consistent with the trends shown by the PDFs. Thick, rolled-up layers of mostly unmixed jet fluid and mostly unmixed crossflow fluid that are transported by the large structures yield the high-probability wings of the PDFs. The jetlike plumes that eject fluid out of the jet core also contribute to this form of PDF. Smaller scale mixing at the interface of the layers and around the edges of smaller structures in the flowfield results in the remaining range of intermediate intensity ratios that exhibit much smaller probabilities. However, because the spatial resolution of these measurements is not sufficient to resolve the diffusion, that is, Batchelor, scale, the intermediate intensity ratios

measured here may represent fluid that is at least well stirred within the volume imaged onto a particular CCD pixel and not necessarily mixed on a molecular level.

Other significant conclusions that can be made based on the current results are as follows.

1) The best instantaneous mixing in the near-field region of the jet occurs in the center of the wake region slightly below the jet centerline. PDFs show that the instantaneous levels of mixing in this flowfield are relatively poor in most regions other than in the wake. Significant probabilities of unmixed fluid (whether jet or crossflow) persist in these other regions. The level of mixing improves with downstream distance from the Mach disk.

2) A relatively large portion (perhaps a majority) of the total jet fluid bypasses the Mach disk through the upstream edge of the barrel shock. This fluid retains a significant fraction of its momentum as it passes through the barrel shock at an oblique angle and is able to penetrate quite deeply into the crossflow. The penetration of this high-momentum jet fluid contributes to the formation of large turbulent structures in the mixing region above the jet centerline. These structures seem to entrain considerable amounts of crossflow fluid into the jet and affect the ultimate penetration of the jet.

3) The counter-rotating streamwise vortex pair plays an important role in the scalar mixing levels in the TJISF flowfield. This vortex structure transports jet fluid down toward the wake and entrains crossflow fluid from below up into the jet. The vortex pair is undoubtedly largely responsible for the relatively high levels of mixing in the wake region below the jet.

4) The counter-rotating streamwise vortex pair develops in an asymmetric manner immediately downstream of the Mach disk. The asymmetric nature of this structure appears to be sensitive to disturbances in the barrel shock region that affect the shape of that portion of the jet cross section that contains the high-momentum jet fluid that bypassed the Mach disk. The streamwise vortex pair gradually becomes more symmetric as it travels farther downstream from the Mach disk.

5) Distinct large-scale structures are seen to extend from the jet far into the crossflow and to engulf large portions of crossflow fluid, contributing greatly to the near-field mixing of the jet with the crossflow. These structures vary in size and spacing along the jet–crossflow interface. The rotation direction of most of these eddies indicates that the jet fluid at the interface usually is moving faster than the crossflow fluid at the interface. Many mushroom-shaped jet plumes, probably consisting of vortex rings, also extend out of the jet boundary in various directions.

References

[1]Gruber, M. R., "An Experimental Investigation of Transverse Injection from Circular and Elliptical Nozzles into a Supersonic Crossflow," Ph.D. Dissertation, Dept. of Mechanical and Industrial Engineering, Univ. of Illinois, Urbana, IL, Jan. 1996.

[2]Margason, R. J., "Fifty Years of Jet in Cross Flow Research," *AGARD Computational and Experimental Assessment of Jets in Crossflow*, No. 534, Winchester, England, U.K., 1993.

[3]Messersmith, N. L., and Dutton, J. C., "Characteristic Features of Large Structures in Compressible Mixing Layers," *AIAA Journal*, Vol. 34, No. 9, 1996, pp. 1814–1821.

[4]Clemens, N. T., and Mungal, M. G., "Large-Scale Structure and Entrainment in the Supersonic Mixing Layer," *Journal of Fluid Mechanics*, Vol. 284, 1995, pp. 171–216.

[5]Brown, G. L., and Roshko, A., "On Density Effects and Large Structure in Turbulent Mixing Layers," *Journal of Fluid Mechanics*, Vol. 64, Pt. 4, 1974, pp. 775–816.

[6]Zukoski, E. E., and Spaid, F. W., "Secondary Injection of Gases into a Supersonic Flow," *AIAA Journal*, Vol. 2, No. 10, 1964, pp. 1689–1696.

[7]Schetz, J. A., and Billig, F. S., "Penetration of Gaseous Jets Injected into a Supersonic Stream," *Journal of Spacecraft and Rockets*, Vol. 3, No. 11, 1966, pp. 1658–1665.

[8]Papamoschou, D., and Hubbard, D. G., "Visual Observations of Supersonic Transverse Jets," *Experiments in Fluids*, Vol. 14, No. 6, 1993, pp. 468–471.

[9]Rothstein, A. D., and Wantuck, P. J., "A Study of the Normal Injection of Hydrogen into a Heated Supersonic Flow Using Planar Laser-Induced Fluorescence," AIAA Paper 92-3423, Jan. 1992.

[10]Fletcher, D. G., and McDaniel, J. C., "Laser-Induced Iodine Fluorescence Technique for Quantitative Measurement in a Nonreacting Supersonic Combustor," *AIAA Journal*, Vol. 27, No. 5, 1989, pp. 575–580.

[11]Gallard, R., Geffroy, P., Jacquin, L., and Losfeld, G., "Etude Experimentale Sur Les Interactions Entre Un Jet Supersonique Chauffe Transversal Et Un Ecoulement Supersonique Externe," *AGARD Computational and Experimental Assessment of Jets in Crossflow*, Winchester, England, U.K., 1993, pp. 39.1–39.12.

[12]Eklund, D. R., Northam, G. B., Dancey, C. L., and Wang, J. A., "Computational/Experimental Investigation of Staged Injection into a Mach 2 Flow," *AIAA Journal*, Vol. 32, No. 5, 1994, pp. 907–916.

[13]Santiago, J. G., and Dutton, J. C., "Velocity Measurements of a Jet Injected into a Supersonic Crossflow," *Journal of Propulsion and Power*, Vol. 13, No. 2, 1997, pp. 729–735.

[14]Santiago, J. G., and Dutton, J. C., "Crossflow Vortices of a Jet Injected into a Supersonic Crossflow," *AIAA Journal*, Vol. 35, No. 5, 1997, pp. 915–917.

[15]Santiago, J. G., "An Experimental Study of the Velocity Field of a Transverse Jet Injected into a Supersonic Crossflow," Ph.D. Dissertation, Dept. of Mechanical and Industrial Engineering, Univ. of Illinois, Urbana, IL, Aug. 1995.

[16]Lee, M. P., McMillin, B. K., Palmer, J. L., and Hanson, R. K., "Planar Fluorescence Imaging of a Transverse Jet in a Supersonic Crossflow," *Journal of Propulsion and Power*, Vol. 8, No. 4, 1992, pp. 729–735.

[17]Hermanson, J. C., and Winter, M., "Mie Scattering Imaging of a Transverse, Sonic Jet in Supersonic Flow," *AIAA Journal*, Vol. 31, No. 1, 1993, pp. 129–132.

[18]Gruber, M. R., Nejad, A. S., Chen, T. H., and Dutton, J. C., "Mixing and Penetration Studies of Sonic Jets in a Mach 2 Freestream," *Journal of Propulsion and Power*, Vol. 11, No. 2, 1995, pp. 315–323.

[19]VanLerberghe, W. M., "Large-Scale Structure and Mixing in a Sonic Transverse Jet Injected into a Supersonic Crossflow," Ph.D. Dissertation, Dept. of Mechanical and Industrial Engineering, Univ. of Illinois, Urbana, IL, Sept. 1995.

[20]Segal, C., Haj-Hariri, H., and McDaniel, J. C., "A Numerical Investigation of Hydrogen Combustion in a Mach 2 Airflow," AIAA Paper 92-0341, Jan. 1992.

[21]Carroll, B. F., "A Numerical and Experimental Investigation of Multiple Shock Wave/Turbulent Boundary Layer Interactions in a Rectangular Duct.," Ph.D. Dissertation, Dept. of Mechanical and Industrial Engineering, Univ. of Illinois, Urbana, IL, Aug. 1988.

[22]Lozano, A., Yip, B., and Hanson, R. K., "Acetone: A Tracer for Concentration Measurements in Gaseous Flows by Planar Laser-Induced Fluorescence," *Experiments in Fluids*, Vol. 13, No. 6, pp. 369–376, 1992.

[23]Hanson, R. K., Seitzman, J. M., and Paul, P. H., "Planar Laser-Fluorescence Imaging of Combustion Gases," *Applied Physics B*, Vol. 50, No. 6, 1990, pp. 441–454.

[24]Smith, S. H., and Mungal, M. G., "Mixing, Structure and Scaling of the Jet in Crossflow," *Journal of Fluid Mechanics*, Vol. 357, 1998, pp. 83–122.

[25]Breuer, G. M., and Lee, E. K. C., "Fluorescence Decay Times of Cyclic Ketones, Acetone, and Butanal in the Gas Phase," *Journal of Physical Chemistry*, Vol. 75, No. 7, 1971, pp. 989, 990.

[26]Ghandhi, J. B., and Felton, P. G., "On the Fluorescent Behaviour of Ketones at High Temperatures," *Experiments in Fluids*, Vol. 21, No. 2, 1996, pp. 143, 144.

[27]Grossmann, F., Monkhouse, P. B., Ridder, M., Sick, V., and Wolfrum, J., "Temperature and Pressure Dependence of the Laser-Induced Fluorescence of Gas-Phase Acetone and 3–Pentanone," *Applied Physics B*, Vol. 62, No. 3, 1996, pp. 249–253.

[28]Lee, J. G., and Santavicca, D. A., "Fiber-Optic Probe for Laser-Induced Fluorescence Measurements of the Fuel-Air Distribution in Gas-Turbine Combustors," *Journal of Propulsion and Power*, Vol. 13, No. 3, 1997, pp. 384–387.

[29]Ossler, F., and Alden, M., "Measurements of Picosecond Laser Induced Fluorescence from Gas Phase 3–Pentanone and Acetone: Implications to Combustion Diagnostics," *Applied Physics B*, Vol. 64, No. 4, 1997, pp. 493–502.

[30]Bryant, R. A., Donbar, J. M., and Driscoll, J. F., "Acetone LIF for Flow Visualization at Temperatures Below 300 K," AIAA Paper 97-0156, Jan. 1997.

[31]Yuen, L. S., Peters, J. E., and Lucht, R. P., "Pressure Dependence of Laser-Induced Fluorescence from Acetone," *Applied Optics*, Vol. 36, No. 15, 1997, pp. 3271–3277.

[32]Broadwell, J. E., and Mungal, M. G., "Molecular Mixing and Chemical Reactions in Turbulent Shear Layers," *Twenty-Second Symposium (International) on Combustion*, Combustion Inst., Pittsburgh, PA, 1988, pp. 579–587.

[33]Broadwell, J. E., and Breidenthal, R. E., "Structure and Mixing of a Transverse Jet in Incompressible Flow," *Journal of Fluid Mechanics*, Vol. 148, 1984, pp. 405–412.

[34]Clemens, N. T., "An Experimental Investigation of Scalar Mixing in Supersonic Turbulent Shear Layers," Mechanical Engineering Dept., HTGL Rept. T-274, Stanford Univ., Stanford, CA, June 1991.

G. M. Faeth
Editor-in-Chief